metals

MDPI

Article

Design of Cobalt-Free High-Entropy Alloy Binder for WC-Base Cemented Carbides

Ivan Goncharov [1], Vera Popovich [2], Marcel Sluiter [2], Anatoly Popovich [3] and Maurizio Vedani [1,*]

[1] Department of Mechanical Engineering, Politecnico di Milano, 20156 Milano, Italy; ivan.goncharov@polimi.it
[2] Department of Materials Science and Engineering, Delft University of Technology, 2628 Delft, The Netherlands; v.popovich@tudelft.nl (V.P.); m.h.f.sluiter@tudelft.nl (M.S.)
[3] Institute of Machinery, Materials, and Transport, Peter the Great St. Petersburg Polytechnic University, St. Petersburg 195251, Russia; director@immet.spbstu.ru
* Correspondence: maurizio.vedani@polimi.it

Abstract

Cemented carbides are essential in applications requiring exceptional hardness and wear resistance. However, the reliance on cobalt as a binder raises concerns related to cost, supply security, and health. High-entropy alloys (HEAs) are promising cobalt-free binders offering favorable mechanical properties and potential grain-growth control. This work presents a new approach for the development of Co-free WC-based cemented carbide employing an HEA binder designed through CALPHAD-guided simulations. An optimized composition corresponding to Al5Cr5Cu10Fe35Mn10Ni35 (at%) alloy is predicted to be FCC-dominant with minimal σ-phase formation and good compatibility with WC. A preliminary batch of powder of the proposed binder was produced by blending elemental powders, arc remelting, and ultrasonic atomization, yielding predominantly spherical particles with a dendritic microstructure. WC–HEA composites (WC–12 wt% HEA) were then prepared by ball milling, pressing, vacuum sintering, and sinter-HIP for a first evaluation of the microstructure and achievable hardness. The microstructure exhibited residual porosity without significant WC grain coarsening. XRD analyses showed the dominant presence of WC, along with FCC and M_3W_3C phases (M mainly Fe and Mn), indicating thermal interaction between the binder and WC. Despite these effects, the composite achieved a hardness of 1913 HV and retained a fine WC grain size (0.86 μm). The proposed design approach allowed the definition of a promising Co-free binder composition based on HEA with the expected microstructure, which will need further evaluation, especially aimed at investigating toughness properties as a function of the WC content.

Keywords: high-entropy alloys; cemented carbides; WC; CALPHAD; microstructure; ultrasonic atomization

Academic Editor: Jiro Kitagawa

Received: 12 February 2026
Revised: 5 March 2026
Accepted: 10 March 2026
Published: 12 March 2026

1. Introduction

Cemented carbides (hardmetals) consist of a hard carbide phase dispersed in a tougher metallic binder. These materials are characterized by exceptional hardness and wear resistance, making them ideal in demanding operational environments. Tungsten carbide–cobalt (WC–Co) is one of the most widely used cemented carbide systems for applications such as wear-resistant components, cutting tools, molds, and mining equipment. The ternary W–Co–C system and the pseudo-binary WC–Co system, where WC and Co are the primary phases, have been extensively studied [1]. WC–Co composites are widely used in industry for their excellent mechanical properties and cutting performance. These

properties include high hardness, compressive strength, fracture toughness, and transverse rupture strength, as well as excellent wear and corrosion resistance [2–5]. The main factors influencing mechanical properties are the binder phase fraction, carbide grain size and distribution, and carbon content [6].

Cobalt remains the predominant binder in cemented carbides because of its superior wetting behavior with WC and its favorable mechanical properties, including strength and toughness. However, cobalt presents critical challenges. Its scarcity makes it expensive, and several programs classify it as highly toxic and carcinogenic [7–10]. These health and environmental concerns make cobalt less desirable for future use. Ni has attracted significant attention as an alternative binder due to its structural and property similarities to cobalt, along with its excellent corrosion resistance. Its FCC structure also improves fracture toughness [11,12]. However, the higher stacking fault energy of Ni results in lower work hardening rates, reducing hardness in WC–Ni cemented carbides. As an alternative to Co and Ni, Fe offers increased hardness in the WC–Fe system and inhibits grain growth, but has poor corrosion resistance and high carbon affinity, which may lead to the formation of the η phase (M_6C), thus limiting efficient applications as a matrix for cemented carbides [13].

Further development resulted in more complex systems, incorporating multiple alloying elements for the binder such as Fe–Ni, Fe–Ni–Co, and Fe–Ni–Co–Cr. Such multicomponent binders eventually lead to the formation of secondary complex carbides and intermetallic phases. In addition, a new approach has been developed, involving the substitution of cobalt-bearing binders with multicomponent alloys known as high-entropy alloys (HEAs). These alloys contain at least five components, with 5–35 at% of each element [14]. HEAs usually have a single-phase microstructure with a densely packed crystal structure (FCC, BCC, or HCP) featuring high hardness [15], high-temperature strength [16], ductility, and even shape-memory effects [17,18]. The crystal lattice distortions in HEAs largely prevent diffusional mass transfer, thus improving phase stability. Moreover, certain HEA systems can have a fairly low melting point, enabling a reduction in the sintering temperature of cemented carbides compared to Co [19] and preventing WC grain growth [20–23]. Among various HEAs, extensive research has been dedicated to the AlCoCrCuFeNi, CoCrCuFeNiMo and AlFeCoNiCrTi systems [24–30]. HEAs belonging to the AlCoCrCuFeNi system generally consist of a combination of FCC and BCC phases, the BCC phase featuring a higher melting point than the FCC phase. It has been demonstrated that modifications of the above HEA composition can lead to different fractions of the two phases. Cu is an FCC-phase stabilizer whereas Al and Cr are BCC formers. The BCC phase undergoes decomposition and ordering, especially enhancing the aluminum content, resulting in a BCC-based B2 ordered phase. Due to the difference in the atomic size, the lattice parameter of the FCC phase decreases with decreasing Al. On the contrary, the lattice parameter of the BCC phase remains substantially the same with limited variation of the components [31]. Substitution of Co in HEAs has been also investigated [32–34]. In an equiatomic system (except for Al), Mn stabilizes the BCC structure, reduces Cu segregation, and enhances the interface bonding with WC [34]. Based on these findings, it was understood that Co could potentially be replaced primarily with Mn in HEAs, resulting in equiatomic or non-equiatomic Co-free compositions based on the AlCrCuFeMnNi system.

Several works [20–23,32,35,36] reported a grain-growth inhibition effect of HEAs during sintering with WC, resulting in finer WC grains in comparison with WC–Co compositions prepared and sintered under the same conditions. This is mainly associated with the sluggish diffusion in HEAs, due to their high activation energy for diffusional phenomena. Finally, a side effect related to the peculiar crystal structure of HEAs consists in the decreased wettability with the hard phases, especially reported for some Al-bearing

HEA binders [28]. This effect is mainly due to the sluggish diffusion effect and the extensive lattice distortion (further amplified by ball milling processing), that make some HEA binders underperform in the sintering stage. To overcome this concern for the most demanding applications, several additives have been proposed to improve the wettability of HEAs toward WC hard phases, as reviewed by Fan et al. [24].

2. Materials and Methods

Phase stability simulations were conducted using Thermo-Calc (version 2023a) using the TCHEA2 database. The widely studied AlCrCoCuFeNi system was chosen as the starting point, initially replacing Co with Mn. The equilibrium state and amount of phases were calculated at the reference temperatures of 900 °C, 600 °C, and 400 °C for the candidate alloys, targeting the highest amount of FCC and the lowest amount of s-phase, under the hypothesis of solidification conditions according to equilibrium or to the Scheil–Gulliver model [37,38]. It should be specified that 400 °C was considered as the lowest temperature for the evaluation of equilibrium phase stability that could be reached under realistic industrial situations, especially considering the sluggish diffusion rate of HEAs. Therefore, data referring to this lowest temperature have to be considered as a trend achievable only upon long holding times, hardly indicative of a condition reached after the investigated processing routes.

Elemental powders consisting of Al, Cr, Cu, Fe, Mn, Ni with 99.9% purity and particle size lower than 45 µm, supplied by Sigma-Aldrich, were blended to the target compositions, cold pressed, and arc-remelted in water-cooled copper molds to obtain rods for the atomization process. Ultrasonic atomization was performed with a metal atomization Amazemet rePowder prototyping platform allowing the synthesis of custom alloy powder in small batches using a molybdenum sonotrode, as depicted in Figure 1. Powder morphology and microstructure were examined by a field emission-scanning electron microscope FE-SEM (ZEISS SIGMA 500, Carl Zeiss AG, Oberkochen, Germany). Sections for microstructural analysis were prepared by mounting and polishing.

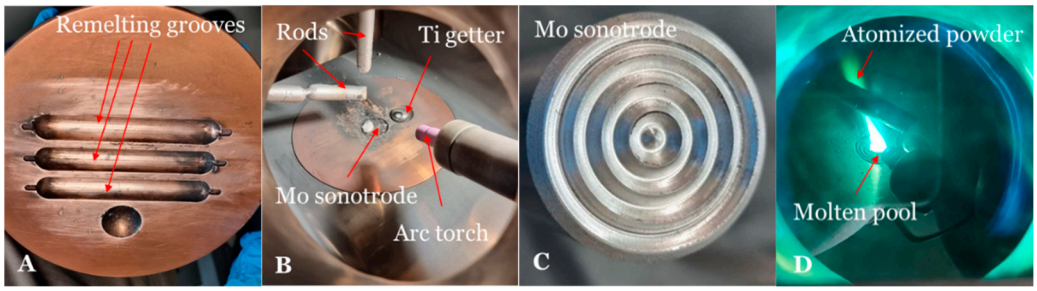

Figure 1. Experimental steps adopted for powder atomization: (**A**) The mold containing grooves for bar remelting; (**B**) setup of the atomizing chamber; (**C**) surface of sonotrode; (**D**) ultrasound atomization process.

HEA powder was then mixed with WC (average grain size 800 nm, supplied by FILMS S.p.A, Anzola d'Ossola, Italy) by ball milling, to form a WC-12 wt% HEA blend. Amongst the possible standard fractions of hard ceramic particles, a WC-lean fraction was selected to better highlight the properties and contribution of the binder.

The densification route was performed according to a traditional powder metallurgy route consisting in a first step of cold pressing of the powder mixture into bars of size 10 × 10 × 55 mm, followed by a pre-sintering stage at 720 °C under gas flow at 1 m^3/h of a mixture of N_2 + 30 vol% H_2 for 4 h, and vacuum sintering at 1400 °C for 3 h. Subsequent sinter-HIP at 1400 °C and 35 bar of pressure for 20 min was the final stage of consolidation using a Quintus Technologies AB apparatus (Västerås, Sweden). Due to the limited amount

of powder available for this investigation, a systematic optimization of the processing conditions could not be carried out. Therefore, parameters were selected on the basis of previous experience with similar alloys.

The density of the sintered samples was measured by the Archimedes method in accordance with the ASTM B311 standard [39]. Microstructural analysis of the sintered samples was performed after polishing and etching with Murakami's reagent using FE-SEM equipped with an Oxford Instruments Ultim Max 65 detector (Abingdon, UK) for elemental mapping.

Phase composition was studied using a Smartlab II Rigaku X-ray diffractometer (Tokyo, Japan) with Cu-Kα radiation (λ = 1.5406 Å) at a scanning rate of 1° min^{-1}, from 10° to 100°, with a step size of 0.02°. Specimens were tested for a preliminary mechanical characterization by Vickers hardness (HV) measurements with an applied load of 100 kg_f for 15 s on polished surfaces (ASTM C1327-15) [40].

3. Results and Discussion

3.1. Simulation and Optimization of Target High-Entropy Alloy Compositions

Phase-stability simulations were first performed for $Al_{0.5}$CoCrCuFeNi and $Al_{0.5}$CrCuFeMnNi alloys [33]. The phases expected at equilibrium against temperature for these alloys are shown in Figure 2. The plots reveal that the main phases appearing upon solidification for the $Al_{0.5}$CoCrCuFeNi HEA are the two types of L12 FCC crystal structures, labelled as FCC_L12 and FCC_L12#2, that later decompose forming a B2-type BCC (hereafter BCC_B2#2) and σ phase (labelled as SIGMA in ThermoCalc plots). With further decrease of temperature, a significant fraction of secondary phases is formed. In the case of the $Al_{0.5}$CrCuFeMnNi alloy, the FCC_L12 and BCC_B2 are the expected phases right after solidification. While the σ phase appears at a higher temperature than the previous alloy.

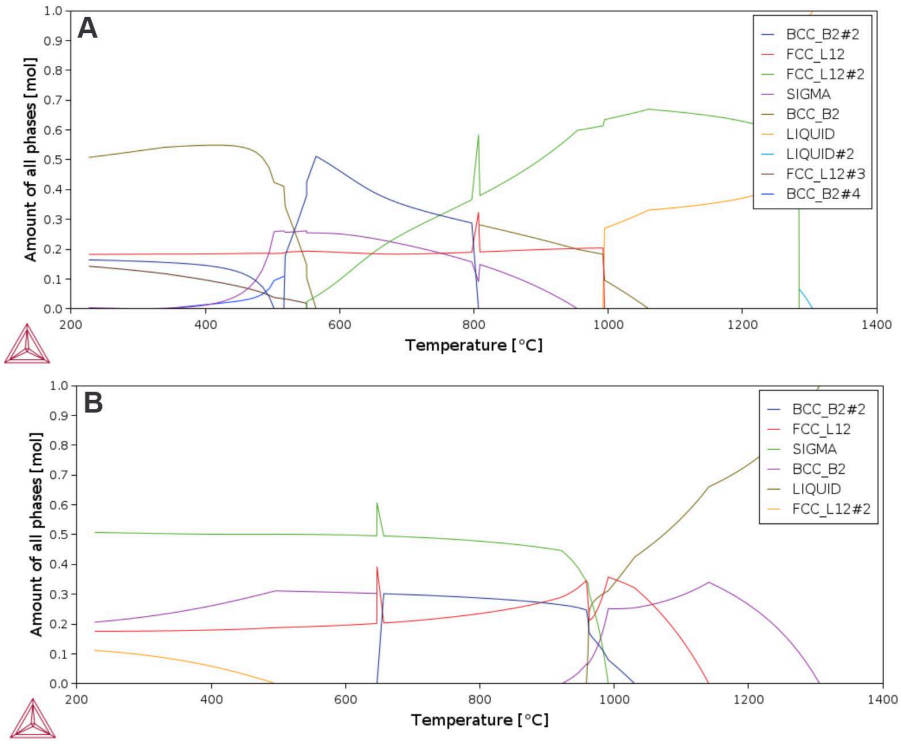

Figure 2. Phase stability under equilibrium according to Thermocalc simulation: (**A**) $Al_{0.5}$CoCrCuFeNi HEA; (**B**) $Al_{0.5}$CrCuFeMnNi HEA.

For further iterations, the Co-free $Al_{0.5}CrCuFeMnNi$ was considered as the starting point for the fine tuning of the composition, targeting the formation of a higher fraction of the FCC phase and the reduction of the s phase.

3.1.1. Effects of Elements on Phase Stability

To understand the influence of each element on phase distribution of HEA, several simulations were performed starting from the above-described $Al_{0.5}CrCuFeMnNi$ alloy. Alloy variants were modeled, in which one element at a time was doubled or halved, with corresponding adjustments of the other elements. However, since Al is a very strong BCC stabilizer in the investigated system [33,41], its content was always kept below the equiatomic fraction to achieve an FCC-dominant phase composition.

Figure 3 presents a collection of histograms summarizing the effects of the element fraction on the stability of the phases at the three selected temperature levels. The four main phases that were found in the investigated alloys are FCC L_12, Cu-rich FCC_L12#2, BCC, and SIGMA. Figure 3 shows that an increase of Cr leads to a decrease of FCC, promotes BCC stability, and increases the SIGMA fraction. An increase in Cu content leads to a drop in BCC and SIGMA and promotes even further development of Cu-rich FCC. An increase of Fe raises the FCC fraction while decreasing BCC and SIGMA. Finally, an increase of Mn increases BCC and SIGMA, while Ni promotes a higher fraction of FCC and suppresses BCC and SIGMA.

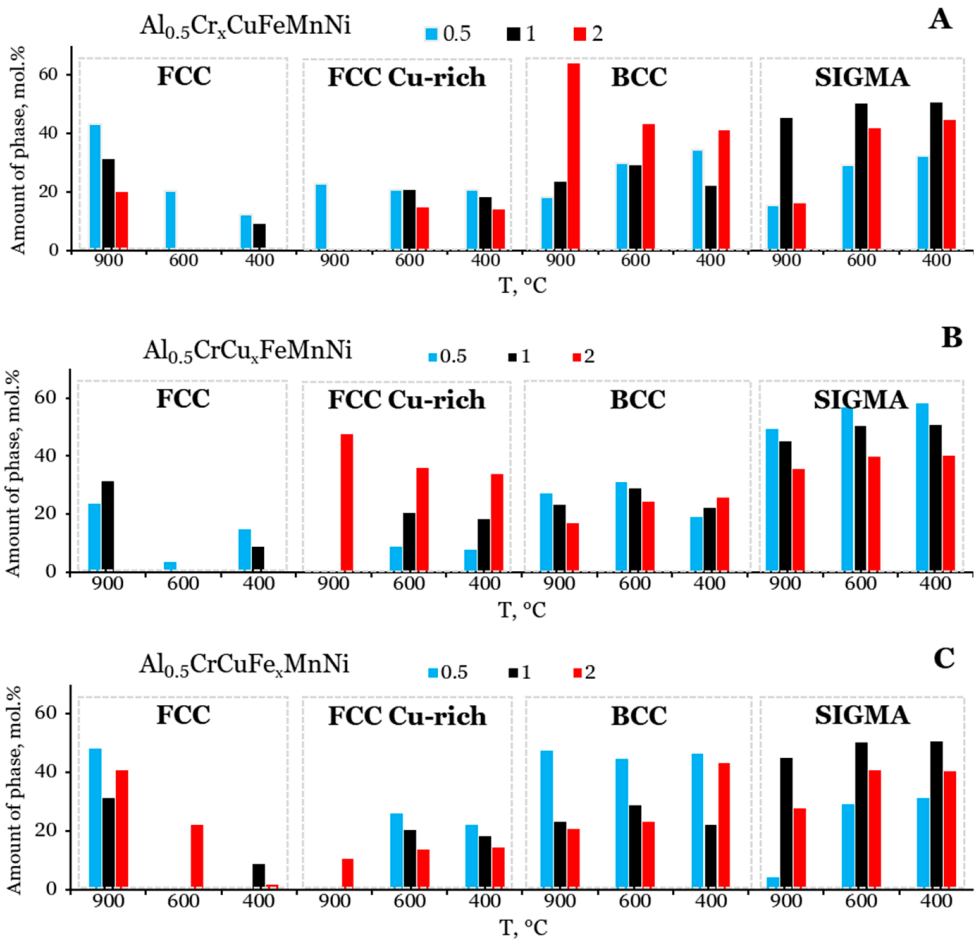

Figure 3. *Cont.*

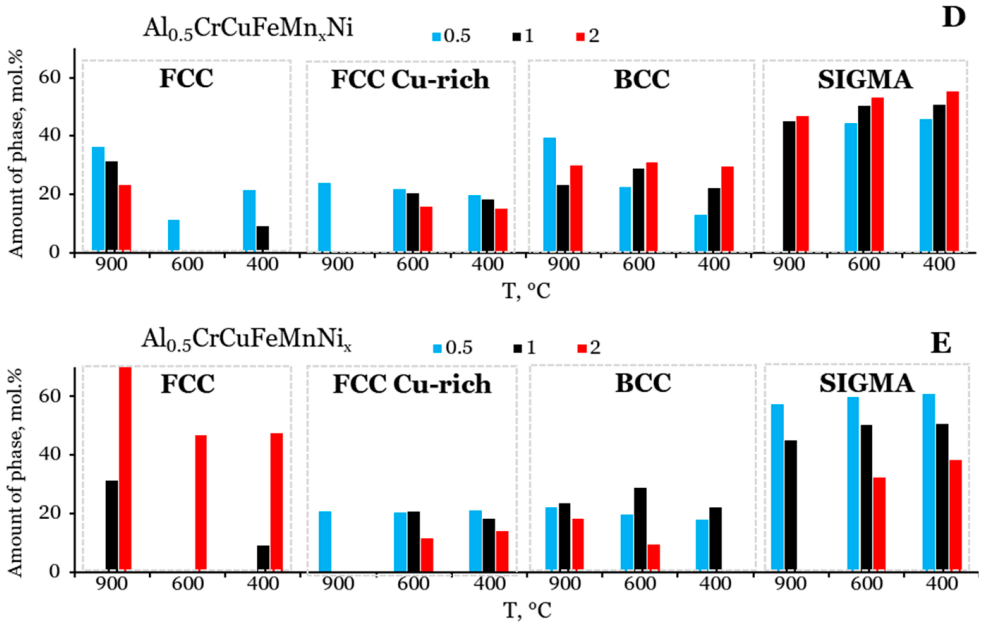

Figure 3. Modifications of phase distribution of $Al_{0.5}CrCuFeMnNi$ HEA resulting from a reduction to 50% (x = 0.5) or an increase by 100% (x = 2) of different elements: (**A**) Cr, (**B**) Cu, (**C**) Fe, (**D**) Mn, (**E**) Ni.

3.1.2. Composition Optimization of HEA

Since the objective of the investigation was to replace Co-bearing binders with HEAs in cemented carbides, one of the main requirements was to target significant toughness properties. Although fracture toughness could not be directly measured in this preliminary investigation, it is well established that FCC or FCC-dominant phase compositions should be preferred to achieve higher toughness properties [19–22,24]. In addition, the concentration of elements was locked within the range of 5–35 at%, which complies with the definition of HEA. Further requirements for the target composition were the absence (or presence in very limited amount) of s phase and the stability of the binder when it is combined with WC.

Following the evaluation presented in Section 3.1.1 on the impact of composition on phase fractions, it was determined that Ni and Fe are the most influential elements for the predominance of the FCC phase. Therefore, for the first iteration, Ni was doubled, resulting in $Al_{0.5}CrCuFeMnNi_2$ (HEA 2-1) composition. Figure 4A shows that the amount of FCC increased, as expected. However, the selected composition still shows some residual BCC. In addition, a substantial amount of s phase is still predicted, corresponding to 32.2 and 38.5 mol% at 600 °C and 400 °C, respectively. For sake of clarity, it must be recalled that the data referring to the 400 °C isotherm were taken to collect additional information about the trend of the phase decomposition. However, considering the limited diffusivity of elements at that temperature, it is unlikely that under real processing conditions such a phase equilibrium can be reached.

As mentioned above, Cr is one of the elements that stabilizes BCC, in turn suppressing FCC. Therefore, a second iteration consisted of setting Ni to 35 at%, and halving Cr, resulting in the $Al_{8.3}Cr_{8.3}Cu_{16.1}Fe_{16.1}Mn_{16.1}Ni_{35}$ composition (hereafter called HEA 2-2). As shown in Figure 4B, FCC increased even further, resulting in an amount of 90.5 and 49.8 mol% at 900 °C and 600 °C, respectively. In addition, there was a substantial decrease in s phase, from 32.2% to 15.5% at 600 °C. The composition of the residual BCC showed a high Al concentration, and the s phase mainly contained Fe and Mn, with a small amount of Ni.

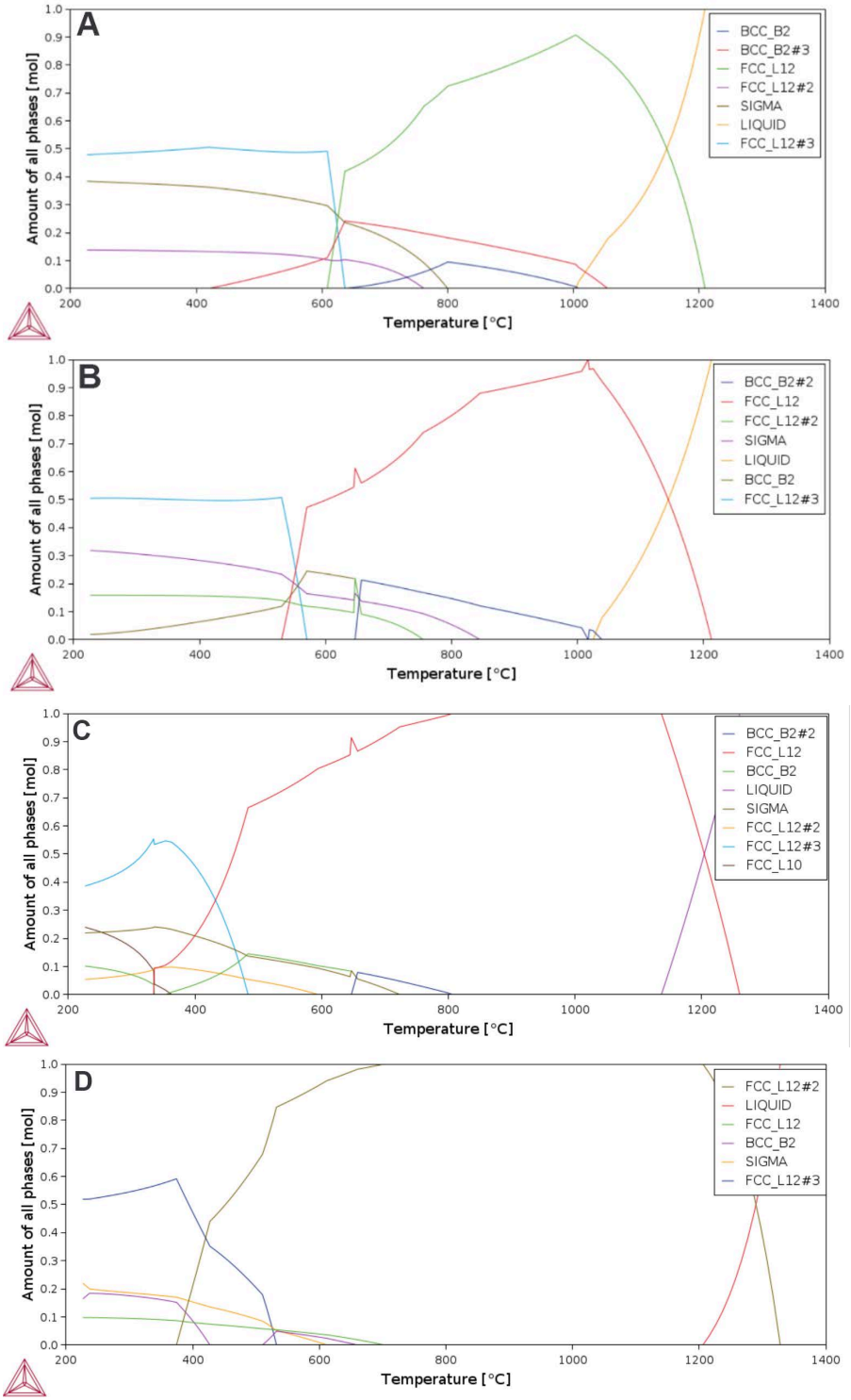

Figure 4. Phase stability under equilibrium according to Thermocalc simulation for the investigated HEAs. (**A**) HEA 2-1; (**B**) HEA 2-2; (**C**) HEA 2-3; (**D**) HEA 2-4.

In a further optimization step, a reduction in Al and Cr and an increase of Fe was evaluated. Al and Cr were minimized to 5%, and Fe was raised at the cost of the share of Cu, resulting in a new composition: $AlCr_5Cu_{12}Fe_{23}Mn_{20}Ni_{35}$ (hereafter called HEA 2-3). The corresponding phase evolution against temperature is given in Figure 4C. The phase balance now resulted in a higher amount of FCC phase, that decomposed at lower temperatures into FCC_L12#3. The remaining phases were the Mn-rich BCC and an even lower fraction of the s phase.

Finally, by fixing the amount of Fe to 35% at the cost of Mn and Cu, which were equalized at 10%, a fourth iteration was considered, leading to the chemical composition $Al_5Cr_5Cu_{10}Fe_{35}Mn_{10}Ni_{35}$ (hereafter called HEA 2-4). According to Figure 4D, HEA 2-4 is expected to keep a single-phase structure down to 700 °C, and remain FCC dominant, with a negligible amount of s phase at 600 °C.

For the sake of precision, in both HEA 2-3 and HEA 2-4, distinct FCC_L12 phases are depicted in the plot. Their composition differs in Cu content. For instance, for HEA 2-3 at 600 °C the main phase is FCC_L12 that consists of $Ni_{36.9}Fe_{24}Mn_{18.6}Cu_{14.5}Cr_{2.7}Al_{3.3}$, while at 400 °C it decomposes, segregating FCC_L12#1, which consists of $Cu_{92.7}Mn_{3.8}Ni_{3.4}Al_{0.1}$. Cu segregation has already been observed in HEAs; it was attributed to the positive mixing enthalpy with Cr and Fe and the negative mixing enthalpy with Ni. It was reported that Cu segregation could be mitigated by increasing the solidification rate [42,43].

A comparative evaluation of the resulting phases for the above-described alloys was collated as in Figure 5A. The best expected condition, corresponding to the highest amount of FCC and the lowest amount of s phase is met for the HEA2-4 alloy defined by the fourth iteration, that corresponds to the composition $Al_5Cr_5Cu_{10}Fe_{35}Mn_{10}Ni_{35}$ at%.

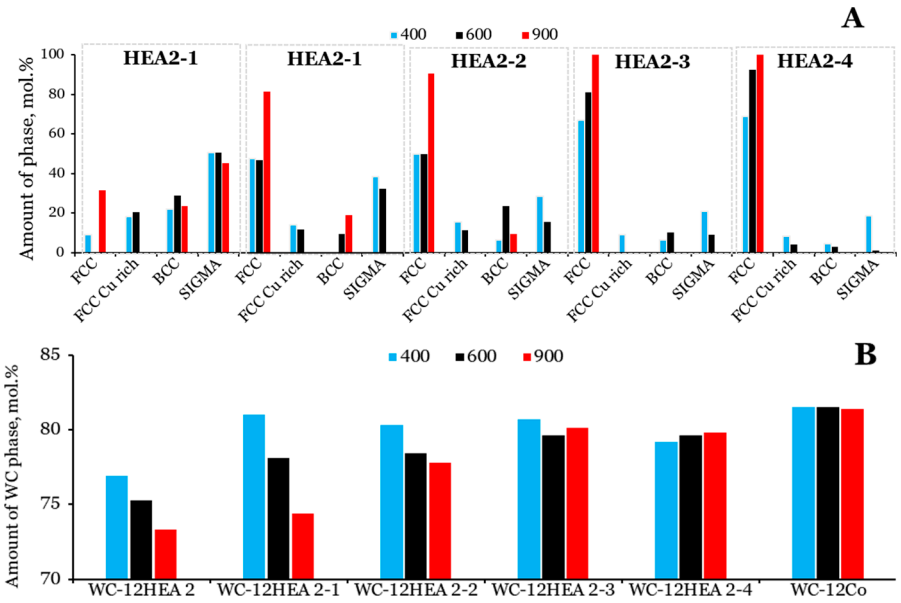

Figure 5. Evaluation of the stability of expected main phases of the proposed HEAs (**A**) and stability of the WC phase when combined with 12 wt% of the proposed HEAs (**B**).

Figure 5B shows a comparative chart of the stability of WC phase in equilibrium within the WC-AlCrCuFeMnNi system, with the hypothesis of producing composites containing WC and 12 wt% of HEA binder using one of the proposed HEAs. For comparison purposes, a standard WC-12Co cemented carbide was also included in the evaluation. The stability of the WC phase was evaluated by calculating the residual amount of unreacted WC achieved at the indicated temperatures under equilibrium, recalling the assumption that an initial 88 wt% of WC (12 wt% of binder) corresponds to a value of 80.7 mol% of WC and 19.3 mol% of binder. From the simulations, it was demonstrated that the stability of WC is higher with HEA 2-3 and HEA 2-4, in comparison to HEA 2, HEA 2-1, and HEA 2-2. However, the simulation shows that under equilibrium, the stability of WC is slightly lower for the HEAs than for the traditional Co binder.

In conclusion, based on Thermo-Calc simulations, HEA 2-4 is expected to have the most stable phase composition, characterized by an FCC-dominant crystal structure which is a prerequisite for achieving toughness properties required for the final application. The

s phase, a detrimental component promoting alloy brittleness, is expected to form only at equilibrium, below 400 °C, which is unlikely to occur in practical situations. Based on these factors, the HEA 2-4 alloy with composition of $Al_5Cr_5Cu_{10}Fe_{35}Mn_{10}Ni_{35}$ at% was selected for the experimental campaign described below.

3.2. Atomization of theHEA Powder

3.2.1. Pressing of the Raw Powders and Bar Remelting

The first step of the preparation of the HEA 2-4 alloy consisted in blending of the Al, Cr, Cu, Fe, Mn, and Ni pure elemental powders by mechanical mixing, followed by uniaxial cold pressing into cylindrical samples. To improve the integrity and homogeneity of the rods, they were remelted using an electric-arc source in water-cooled copper grooves. Their microstructure exhibited a dendritic structure with a bright phase enriched in Cu, and Mn segregated at the dendrite boundaries (Figure 6C). The average chemical composition of the remelted bars, measured by EDS (Table 1), corresponded to nominal composition with slight losses in Al and Cu. Specifically, it was detected that the dendrite cores featured lower Cu and Mn concentration, whereas the interdendritic areas were depleted in Cr and Fe.

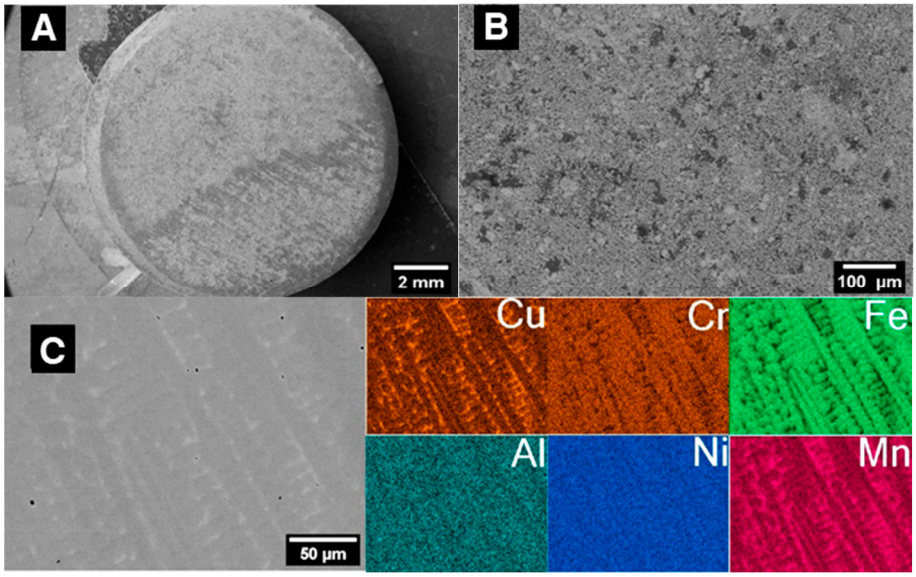

Figure 6. SEM images of general view and section of the pressed HEA 2-4 powder mixture (**A**,**B**); microstructure and elemental maps of the remelted bar (**C**).

Table 1. EDS chemical analysis of the remelted rods of the HEA 2-4 alloy (at%).

Sample	Al	Cr	Cu	Fe	Mn	Ni
Theoretical	5	5	10	35	10	35
Rod (average)	4.5 ± 0.2	5.3 ± 0.1	9.6 ± 0.3	34.9 ± 0.2	10.8 ± 0.5	34.8 ± 0.2
Dendrite cores	4.6 ± 0.2	6 ± 0.3	7.1 ± 0.8	40.5 ± 2.2	8.1 ± 0.8	33.8 ± 0.7
Interdendritic regions	5.3 ± 0.4	1.9 ± 0.2	34.0 ± 4.0	11.8 ± 2.0	19.1 ± 0.5	28.0 ± 2.0

3.2.2. Ultrasonic Atomization of HEA Powder

The HEA rods were ultrasonically atomized with the parameters shown in Table 2. The remelted rods were placed in holders and positioned above the sonotrode (Figure 1B). Once the arc torch was ignited, the end of the rod was melted on the top of the sonotrode to let molten droplets fall on its surface. The 40 Hz ultrasound waves induced by the sonotrode on the melt promoted the outward ejection of smaller droplets, allowing their cooling and

solidification during flight, eventually leading to their collection as solid powder particles in the atomizer chamber. The oxygen contents reported in Table 2 represent the concentration within the atomizer chamber, suggesting a good control of the working environment during the atomization process. SEM images of the atomized powder (Figure 7) revealed the spherical shape of the particles with very small amounts of irregular features and submicron-size satellites. Most of the as-atomized particles (about 90% in mass) passed through a 100 µm sieve.

Table 2. Process parameters for the ultrasonic atomization of the HEA 2-4 powder alloy.

Frequency of sonotrode	40 kHz
Ar flow	5 L/min
Plasma current	250 A
O_2 content (start)	23 ppm
O_2 content (working)	50 ppm

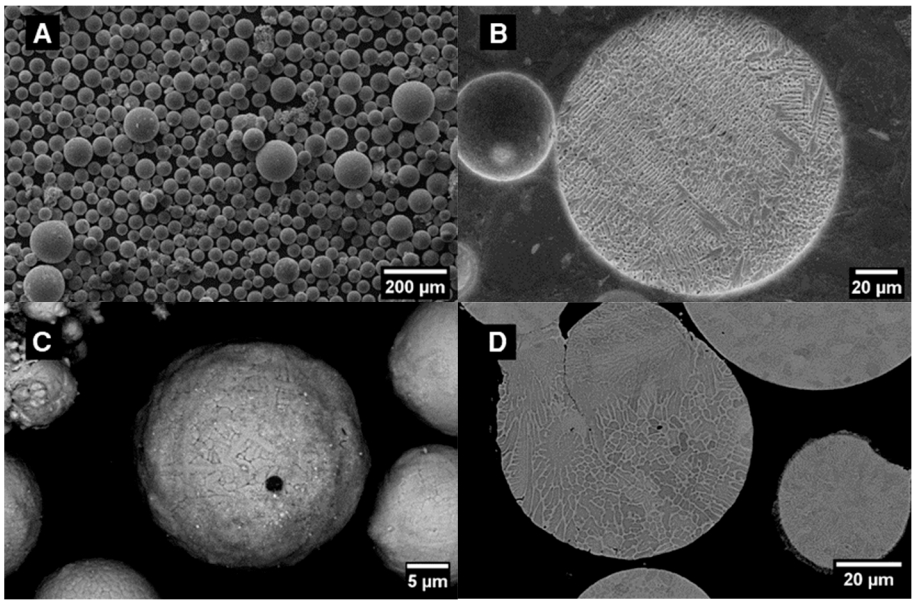

Figure 7. SEM images of the atomized powder: (**A**) general view; (**B**) section of the particle after polishing and etching; (**C**) defect on the particle surface; (**D**) coarser and irregular powder particles.

Sections of the powder particles after polishing and etching revealed a dendritic microstructure with substantial absence of internal porosity or other defects. Elemental mapping of the powder (Figure 8A) collected on sectioned particles showed the segregation of Mn, Al, Cu, and O on the surfaces. In contrast, Cr, Fe, and Ni were distributed within the bulk of the particles. On some powder particles, the occasional presence of Mo was detected (Figure 8B), located mainly within the interdendritic regions. The presence of Mo can be attributed to contamination from the sonotrode during ultrasound atomization.

In addition to submicron satellites and Mo contamination, the predominantly spherical powders produced by ultrasonic atomization exhibited a slight oxidation effect, highlighted by the dark spots in the SEM images in Figure 7C representing Al, Cu, and Mn oxides. The side products of the atomization process included fine powder (<10 µm) with high Cu/Mn/O content and coarse powder (63–150 µm) with a non-spherical shape (Figure 7D).

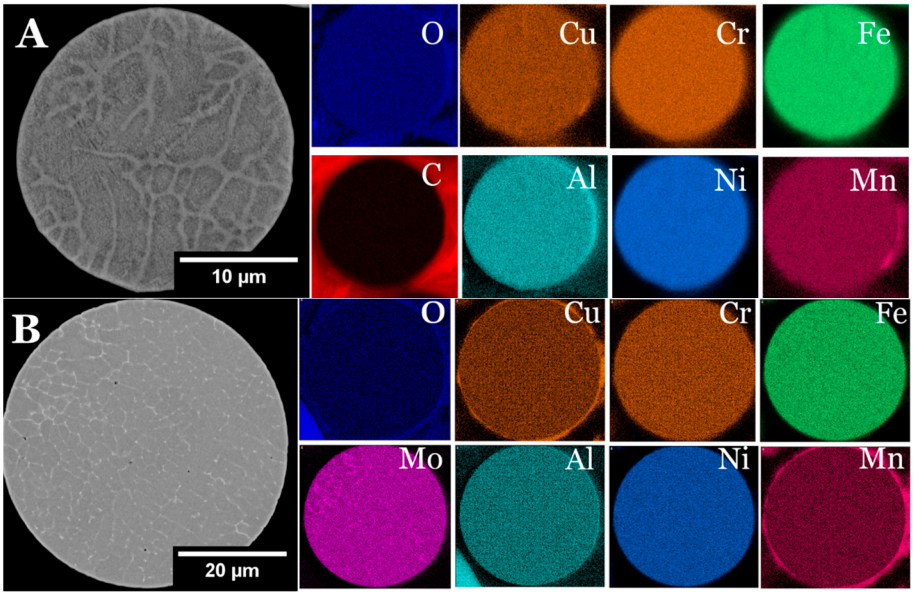

Figure 8. Elemental EDS maps of atomized HEA 2-4 powder: (**A**) standard quality; (**B**) Mo-contaminated particles.

The analysis of the atomized powder revealed elemental losses and compositional shifts, primarily consisting of a decrease in Mn from 10 to 8.9% and Cu from 10 to 8.8%, while the introduction of Mo, due to contamination from the eroded sonotrode, resulted in an average Mo content of 2.6%. Thermo-Calc simulations incorporating the actual composition revealed a higher fraction of s phase at 600 °C (albeit limited to 4%) and suppressed BCC formation until 400 °C, confirming the predominance of the FCC phase also for the modified HEA 2-4 alloy, as depicted in Figure 9. Despite the shift in composition, the WC phase in WC-12HEA composites remained stable, suggesting limited impact on the synthesis of WC–HEA cemented carbides.

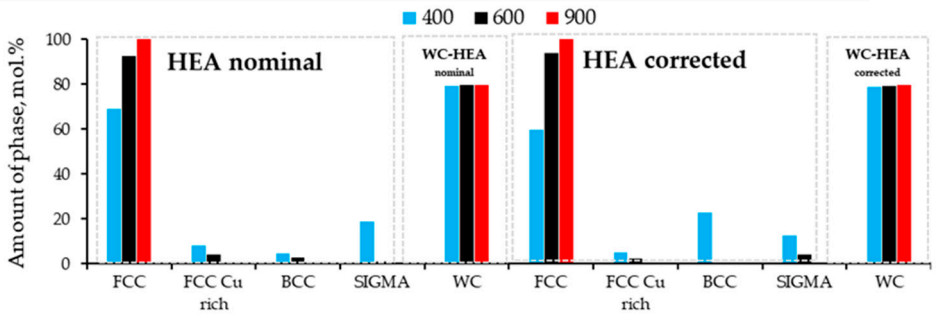

Figure 9. Main phases expected for the HEA 2-4 and WC-12HEA 2-4 composite when comparing the nominal and the measured compositions.

The XRD analysis confirmed the presence of the main FCC phase in the atomized powder (Figure 10). However, a low-intensity peak of secondary phase was also detected, that could be presumably identified as a BCC phase. This peak can be attributed to a non-equilibrium phase generated due to the high cooling rate experienced during atomization of the powder. Indeed, the results of a simulation according to the Scheil–Gulliver model for the HEA2_4 alloy depicted in Figure 11 shows that, in addition to the equilibrium FCC phase, a BCC phase is also expected to form in the last stages of solidification, also leading to a widening of the solidification temperature range (compare to the dashed line referring to equilibrium in Figure 11). For sake of completeness, the same simulation according to the Scheil–Gulliver model was also applied to the corrected composition.

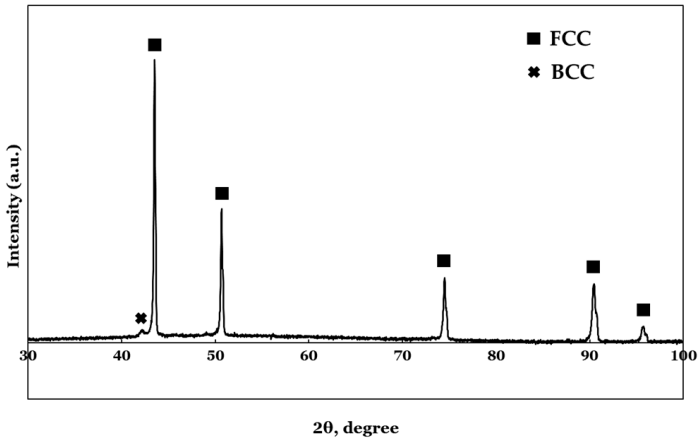

Figure 10. XRD patterns of HEA 2-4 powder.

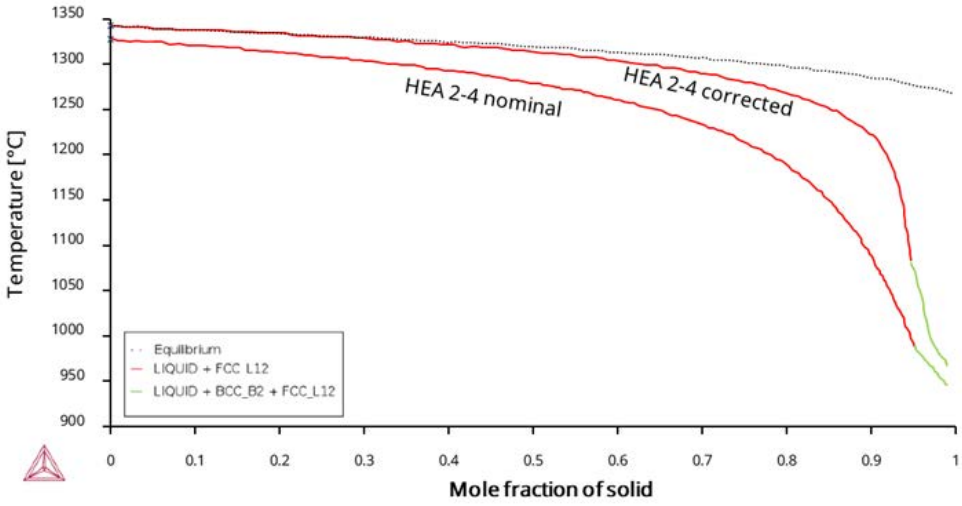

Figure 11. Solidification curve of the nominal and corrected (experimental) HEA 2-4 alloy calculated using ThermoCalc according to the Scheil–Gulliver model.

3.3. Microstructure and Phase Composition of the WC–HEA Cemented Carbides

A powder mixture with nominal composition of WC-12HEA 2-4 (wt%) was prepared by ball milling. The SEM image shown in Figure 12A shows that the WC powder particles are much finer in comparison to the original 10–63 μm HEA powder due to coarsening and flattening, often forming flakes. XRD analysis depicted in Figure 13 revealed the peaks of WC and FCC, which correspond to main FCC phase of the HEA matrix, with no secondary phases observed.

The densification route was performed according to a traditional powder metallurgy route, consisting in a first step of cold pressing of the powder mixture, followed by a pre-sintering stage and a subsequent sinter-HIP at 1400 °C. Rectangular-section bar samples were produced with relative density of 95.8%. It must be specified that a dedicated stage of process optimization would have led to higher density values, exceeding 99% to target practical applications. However, due to the small amount of powder available for this preliminary activity, the selected densification procedure was considered as appropriate.

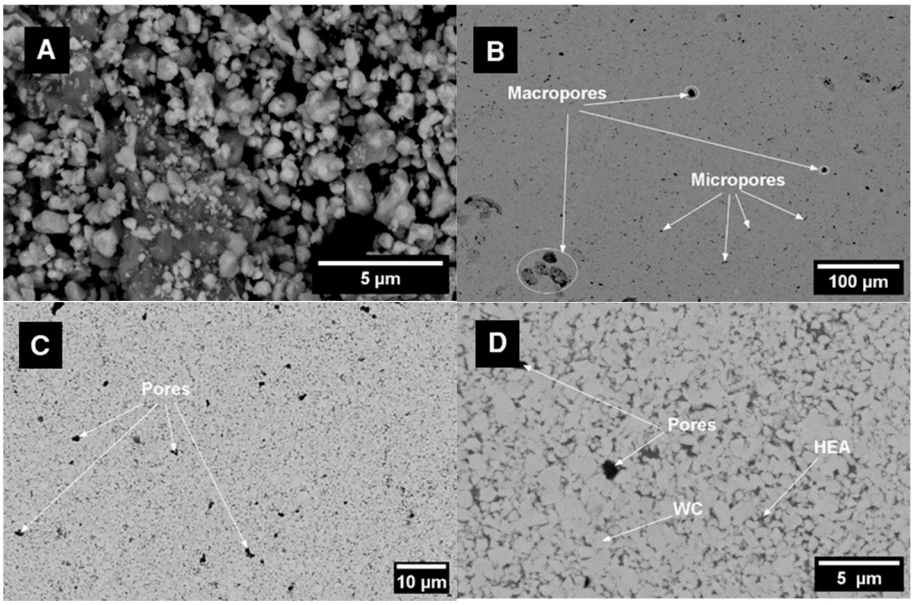

Figure 12. SEM Images of the WC-12HEA alloy: (**A**) powder mixture of the composite powder before sintering; (**B**–**D**) microstructure of sintered samples at increased magnification (from **B**–**D**).

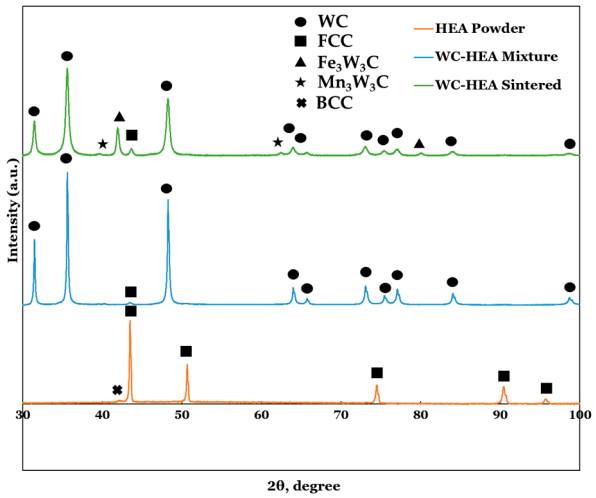

Figure 13. XRD patterns of the as-atomized HEA powder, of the WC–HEA powder blend, and of the sinter-HIPed sample.

Figure 12B illustrates the microstructure of the sinter-HIPed sample, revealing a bimodal pore distribution—sporadic large pores (>20 µm) and more uniformly dispersed micropores (~1 µm). Figure 12C,D demonstrate that no coarse-grained WC areas could be observed, and Table 3 further confirms that the average grain size is close to that of the initial WC powder, which supports the assumption about grain-growth inhibition effect due to HEA sluggish diffusion [20–23,32,35,36].

Concerning the distribution of the metallic binder in the WC–HEA hardmetal, careful observations of the micrographs showed that WC-free areas made only of segregated HEA could be detected. These matrix-bearing regions featured the enrichment in Cr and Fe, as confirmed by EDS elemental maps given in Figure 14. The size of these segregated HEA regions is comparable to the average size of HEA powder particles, which would suggest that during the powder milling, the WC nanoparticles could not evenly be distributed on all the deformed HEA powder particles.

Table 3. Average grain size, density, and hardness of the sinter-HIPed WC-12HEA2_4 sample in comparison with selected hardmetal data (Adapted from Refs. [34,44,45]).

Material	Average WC Grain Size, μm	Relative Density, %	Vickers' Hardness HVn Load, kgf	
WC–HEA2-4	0.86 ± 0.47	95.8	1913 ± 52	100
WC-$Al_{0.5}$CoCrCuFeNi (HEA 1)	0.96 ± 0.59	96.1 ± 0.2	1231 ± 18	100
WC-$Al_{0.5}$CrCuFeMnNi (HEA 2)	1.07 ± 0.66	98.9 ± 0.3	1527 ± 34	100
WC-12Co BJAM [45]	1.60 ± 0.92	99.3 ± 0.1	1222 ± 16	100
WC-10CoCrFeNi [34]	1.16	97.97	1513	30
WC-10AlCoCFeNi [34]	1.62	94.54	1353	30
WC-10CoCrFeNiMo [34]	1.35	97.22	1450	30
WC-10CoCrFeNiMn [34]	1.01	97.56	1562	30
WC-12Co Industrial [44]	n.a.	n.a.	1050–1380	n.a.

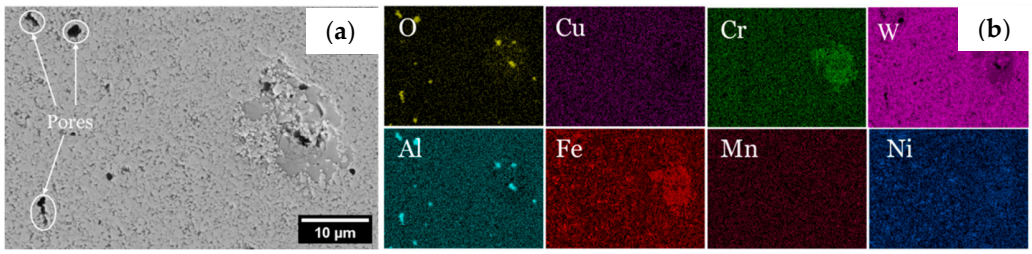

Figure 14. SEM image of the sinter-HIPed sample of WC–HEA hardmetal (**a**) and EDS elemental maps (**b**).

The XRD analysis of the sinter-HIPed sample showed in Figure 13 demonstrates the predominance of the peaks corresponding to WC and the lower-intensity peaks of the FCC binder alloy, in agreement with the XRD spectra of the HEA binder. However, no evidence of the BCC peak is observed in the WC–HEA sinter-HIPed sample, probably due to the very low amount of this phase and the insufficient sensitivity of the XRD analysis. In addition, other peaks appeared that were not present either in the atomized powder or in the WC–HEA powder mixture, which suggests an effect given by the thermally-induced interaction between WC and HEA during the stages of vacuum sintering and sinter-HIPing performed at 1400 °C. These peaks correspond to type-M_3W_3C secondary carbides, often labelled as η-phase [1,23,46], where in the present case M mainly refers to Fe and Mn. It has been reported that, despite their brittleness which may affect fracture toughness when present in relevant amount, M_3W_3C carbides can be beneficial in preventing WC grain growth. During high-temperature consolidation processes, WC particles decompose into W and C atoms that diffuse into the binder and react with elements to create the M_3W_3C phase. The subsequent low atomic mobility within the HEA matrix restricts back diffusion and reprecipitation toward undissolved larger WC particles, thus inhibiting any substantial grain growth of the WC phase [23]. Careful analysis of the microstructure supported by the XRD results enabled confirmation that the s phase was absent from the samples, in agreement with the hypothesis of low elemental diffusivity in the HEA binder, despite the fairly slow cooling rate from the sinter-HIP temperature.

Hardness tests performed on the WC–HEA2-4 bar samples are plotted in Figure 15 together with comparative data collected from the literature for WC-12Co hardmetal conventionally sintered [44] or consolidated by binder jetting additive manufacturing [45]. Unpublished data for WC-based hardmetals manufactured with Co-bearing and Co-free HEAs ($Al_{0.5}$CoCrCuFeNi and $Al_{0.5}$CrCuFeMnNi) are also provided.

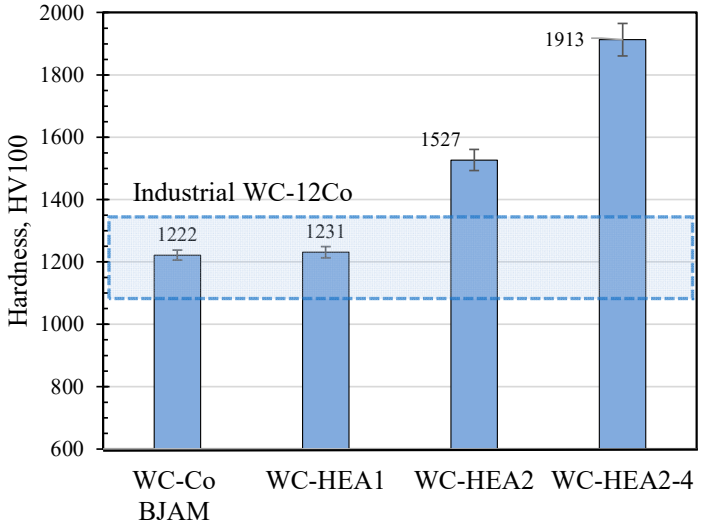

Figure 15. Comparison chart of hardness for the investigated HEA2_4 samples, with data related to other hardmetals (Adapted from Refs. [44,45]).

Further information about grain size and relative density for the same group of materials, as well as results for the WC–HEA compositions studied in [34] are summarized in Table 3. Despite the possible discrepancies arising from the comparison of different batches of alloys, which were also processed according to different routes, the data highlight the high hardness achieved by the proposed HEA 2_4 alloy in comparison with both WC-12Co and other WC–HEA hardmetals presented in the literature. Finally, it must be mentioned that no evidence of crack development was found at the edges of Vickers' indentations, which could suggest a brittle behavior of the investigated WC–HEA hardmetals.

4. Conclusions

In this study a design approach based on CALPHAD modeling is proposed to define a Co-free binder based on a high-entropy alloy (HEA) composition with an FCC-dominant structure, The proposed Co-free HEA, resulting in the formulation $Al_5Cr_5Cu_{10}Fe_{35}Mn_{10}Ni_{35}$ (at%), was subsequently atomized into an experimental small batch of powder, blended with WC by mechanical milling, and consolidated via sinter-HIP to preliminarily evaluate its microstructure, phase stability, and hardness, in view of future and more extensive validation as a binder for WC-based hardmetals.

The atomized particles exhibited a predominantly spherical morphology with a dendritic internal structure. XRD confirmed the main presence of an FCC phase, with a minor fraction of a BCC phase rich in Al at the interdendritic regions. Elemental analysis showed a slight deviation from the nominal composition, attributed to partial evaporation of Mn and Cu during remelting, and slight surface oxidation presumably induced during atomization. The shift in the overall powder composition was such that no substantial difference in phase stability was expected.

The proposed WC-12HEA composite featured a microstructure containing two types of porosity: occasional large pores with size exceeding few tens of micrometers and micropores within the micrometer and sub-micrometer range. No coarse-grained zones were observed in the WC phase, suggesting the HEA's grain-growth inhibition effect. Non-uniform distribution of the metallic phase was detected, with localized segregation of Cr and Fe supposedly due to uneven distribution of the WC particles during powder milling.

XRD analysis of the sintered composite confirmed the dominant presence of WC, along with FCC and M_3W_3C phases (with M mainly representing Fe and Mn), indi-

cating the effects of a thermally induced interaction between WC and the binder alloy during processing.

Hardness measurements demonstrated a substantial improvement over conventional WC-12Co and previously reported WC–HEA composites, highlighting the potential of the proposed alloy for advanced applications. This increase may be attributed to enhanced binder hardness and the suppression of WC grain growth during sintering.

Author Contributions: Conceptualization, I.G., V.P., M.S., A.P. and M.V.; validation, M.S., A.P. and M.V.; investigation, I.G.; writing—original draft preparation, I.G. and M.V.; writing—review and editing, V.P., M.S. and M.V.; supervision, V.P., A.P. and M.V. All authors have read and agreed to the published version of the manuscript.

Funding: This research received no external funding.

Data Availability Statement: The original contributions presented in this study are included in the article. Further inquiries can be directed to the corresponding author.

Acknowledgments: The authors would like to acknowledge the support given by Gian Pietro De Gaudenzi for the sinter-HIP of the samples at HI.Lab, FILMS S.p.A. and Matteo Vanazzi and Mattia Cabrioli (F3nice Srl) for ultrasonic atomization.

Conflicts of Interest: The authors declare no conflicts of interest.

References

1. García, J.; Collado Ciprés, V.; Blomqvist, A.; Kaplan, B. Cemented Carbide Microstructures: A Review. *Int. J. Refract. Met. Hard Mater.* **2019**, *80*, 40–68. [CrossRef]
2. Teppernegg, T.; Klünsner, T.; Kremsner, C.; Tritremmel, C.; Czettl, C.; Puchegger, S.; Marsoner, S.; Pippan, R.; Ebner, R. High Temperature Mechanical Properties of WC–Co Hard Metals. *Int. J. Refract. Met. Hard Mater.* **2016**, *56*, 139–144. [CrossRef]
3. Al-Aqeeli, N.; Saheb, N.; Laoui, T.; Mohammad, K. The Synthesis of Nanostructured WC-Based Hardmetals Using Mechanical Alloying and Their Direct Consolidation. *J. Nanomater.* **2014**, *2014*, 640750. [CrossRef]
4. Zhang, Y.; Hong, S.; Lin, J.; Zheng, Y. Influence of Ultrasonic Excitation Sealing on the Corrosion Resistance of HVOF-Sprayed Nanostructured WC-CoCr Coatings under Different Corrosive Environments. *Coatings* **2019**, *9*, 724. [CrossRef]
5. Kawakami, M. Cemented carbide tools and moulds for wear-resistant applications in Japan. *Int. J. Refract. Met. Hard Mater.* **2024**, *118*, 106477. [CrossRef]
6. Ettmayer, P.; Kolaska, H.; Ortner, H.M. History of Hardmetals. In *Comprehensive Hard Materials*, Salin, V.K., Mari, D., Llanes, L., Eds.; 1st ed.; Elsevier: Amsterdam, The Netherlands, 2014; Volume 1. [CrossRef]
7. REACH Regulation. Available online: https://environment.ec.europa.eu/topics/chemicals/reach-regulation_en (accessed on 25 February 2026).
8. National Toxicology Program. Available online: https://ntp.niehs.nih.gov/ (accessed on 25 February 2026).
9. Simonsen, L.O.; Harbak, H.; Bennekou, P. Cobalt Metabolism and Toxicology-A Brief Update. *Sci. Total Environ.* **2012**, *432*, 210–215. [CrossRef] [PubMed]
10. Armstead, A.L.; Arena, C.B.; Li, B. Exploring the Potential Role of Tungsten Carbide Cobalt (WC-Co) Nanoparticle Internalization in Observed Toxicity toward Lung Epithelial Cells in Vitro. *Toxicol. Appl. Pharmacol.* **2014**, *278*, 1–8. [CrossRef] [PubMed]
11. Steinlechner, R.; De Oro Calderon, R.; Koch, T.; Linhardt, P.; Schubert, W.D. A study on WC-Ni cemented carbides: Constitution, alloy compositions and properties, including corrosion behaviour. *Int. J. Refract. Met. Hard Mater.* **2022**, *103*, 105750. [CrossRef]
12. Li, G.; Peng, Y.; Yan, L.; Xu, T.; Long, J.; Luo, F. Effects of Cr Concentration on the Microstructure and Properties of WC-Ni Cemented Carbides. *J. Mater. Res. Technol.* **2020**, *9*, 902–907. [CrossRef]
13. Kübarsepp, J.; Juhani, K. Cermets with Fe-Alloy Binder: A Review. *Int. J. Refract. Met. Hard Mater.* **2020**, *92*, 105290. [CrossRef]
14. Ye, Y.F.; Wang, Q.; Lu, J.; Liu, C.T.; Yang, Y. High-entropy alloy: Challenges and prospects. *Mater. Today* **2016**, *19*, 349–362. [CrossRef]
15. Feng, C.; Wang, X.; Yang, L.; Guo, Y.; Wang, Y. High Hardness and Wear Resistance in AlCrFeNiV High-Entropy Alloy Induced by Dual-Phase Body-Centered Cubic Coupling Effects. *Materials* **2022**, *15*, 6896. [CrossRef]
16. Razumov, N.; Makhmutov, T.; Kim, A.; Masaylo, D.; Kovalev, M.; Popovich, A. Synthesis and Properties of High-Entropy CoCrFeNiMnWx Alloys. *J. Mater. Res. Technol.* **2023**, *24*, 9216–9224. [CrossRef]

17. Razumov, N.G.; Makhmutov, T.Y.u.; Kim, A.; Goncharov, I.S.; Ozerskoi, N.E.; Silin, A.O.; Mazeeva, A.K.; Popovich, A.A. Structure and Properties of a High-Entropy Ti-Zr-Hf-Ni-Co-Cu Alloy Obtained by Mechanical Alloying and Spark Plasma Sintering. *Metallogr. Microstruct. Anal.* **2021**, *10*, 474–484. [CrossRef]
18. Razumov, N.G.; Makhmutov, T.Y.; Kim, A.; Goncharov, I.S.; Ozerskoi, N.E.; Silin, A.O.; Borisov, E.V.; Starikov, K.A.; Mazeeva, A.K.; Popovich, A.A. Structure and Properties of Ti–Zr–Ni–Co–Cu High-Entropy Alloy After Powder Bed Fusion of Powders Produced by Mechanical Alloying and Plasma Spheroidization. *Trans. Indian Inst. Met.* **2022**, *75*, 2529–2538. [CrossRef]
19. Straumal, B.; Konyashin, I. WC-Based Cemented Carbides with High Entropy Alloyed Binders: A Review. *Metals* **2023**, *13*, 171. [CrossRef]
20. Zhou, P.F.; Xiao, D.H.; Yuan, T.C. Comparison between Ultrafine-Grained WC–Co and WC–HEA-Cemented Carbides. *Powder Metall.* **2017**, *60*, 1–6. [CrossRef]
21. Wang, D.; Li, D.; Ding, Z.; Zhao, B.; Shi, F.; Qi, G. Microstructure and Mechanical Behavior of WC-HEA Cemented Carbide at Various Scales: Molecular Dynamics Simulation and Experimental Study. *Ceram. Int.* **2025**, *51*, 32339–32354. [CrossRef]
22. Huai, J.; Du, J.; Sun, Y.; Xia, Y.; Zhang, P.; Su, G.; Li, Y.; Shi, H.; Huang, J. Effects of High-Entropy Alloy and Fine WC on Microstructure and Properties of WC/CoCrFeNiTi Cemented Carbide. *J. Mater. Eng. Perform.* **2025**, *34*, 24654. [CrossRef]
23. Qiang, F.; Zheng, P.; He, P.; Wang, W.; Zhang, Y.; Han, P.; Wang, K. Insight into Grain Refinement Mechanisms of WC Cemented Carbide with Al0.5CoCrFeNiTi0.5 Binder. *Materials* **2024**, *17*, 4223. [CrossRef]
24. Fan, C.; Sun, J.; Zhao, J.; Yun, X. High entropy alloy bonded cemented carbides: Composition, processing, microstructure, properties and applications. *Ceram. Int.* **2024**, *50*, 37460–37503. [CrossRef]
25. Fan, C.; Sun, J.; Li, X.; Yu, H. Spark Plasma Sintering and Characterization of WC-AlCuMnMoTi Cemented Carbide. *Ceram. Int.* **2025**, *51*, 10000–10013. [CrossRef]
26. Fan, C.; Wu, K.; Liu, Y.; Ni, S.; Jiang, W.; Liu, B.; Chen, Y. Research Status of WC-Based Cemented Carbides with HEA Binders: A Review. *Smart Mater. Manuf.* **2025**, *4*, 100098. [CrossRef]
27. Luo, W.; Liu, Y.; Luo, Y.; Wu, M. Fabrication and Characterization of WC-AlCoCrCuFeNi High-Entropy Alloy Composites by Spark Plasma Sintering. *J. Alloys Compd.* **2018**, *754*, 163–170. [CrossRef]
28. Luo, W.; Liu, Y.; Tu, C. Wetting Behaviors and Interfacial Characteristics of Molten AlxCoCrCuFeNi High-Entropy Alloys on a WC Substrate. *J. Mater. Sci. Technol.* **2021**, *78*, 192–201. [CrossRef]
29. Mueller-Grunz, A.; Alveen, P.; Rassbach, S.; Useldinger, R.; Moseley, S. The Manufacture and Characterization of WC-(Al)CoCrCuFeNi Cemented Carbides with Nominally High Entropy Alloy Binders. *Int. J. Refract. Met. Hard Mater.* **2019**, *84*, 105032. [CrossRef]
30. Zhu, S.; Hui, J.; Qin, J.; Weiwei, D. High Temperature Oxidation Behavior of Spark Plasma Sintered WC-CoCrFeNiAl Hard Alloys. *Int. J. Refract. Met. Hard Mater.* **2023**, *113*, 106157. [CrossRef]
31. Tung, C.C.; Yeh, J.W.; Shun, T.; Chen, S.K.; Huang, Y.S.; Chen, H.C. On the Elemental Effect of AlCoCrCuFeNi High-Entropy Alloy System. *Mater. Lett.* **2007**, *61*, 1–5. [CrossRef]
32. Lin, C.-M.; Tsai, C.-W.; Huang, S.-M.; Yang, C.-C.; Yeh, J.-W. New TiC/$Co_{1.5}CrFeNi_{1.5}Ti_{0.5}$ Cermet with Slow TiC Coarsening During Sintering. *J. Manag.* **2014**, *66*, 2050–2056. [CrossRef]
33. Chen, H.Y.; Tsai, C.W.; Tung, C.C.; Yeh, J.W.; Shun, T.T.; Yang, C.C.; Chen, S.K. Effect of the Substitution of Co by Mn in Al-Cr-Cu-Fe-Co-Ni High-Entropy Alloys. *Ann. Chim. Sci. Mater.* **2006**, *31*, 685–698. [CrossRef]
34. Liang, F.; Du, J.; Su, G.; Zhang, P.; Zhang, C. Investigating the Effect of Al, Mo or Mn Addition to CoCrFeNi Entropy Alloys on the Interface Binding Properties of WC/HEA Cemented Carbides. *Mater. Today Commun.* **2023**, *35*. [CrossRef]
35. Velo, I.L.; Gotor, F.J.; Alcalá, M.D.; Real, C.; Córdoba, J.M. Fabrication and Characterization of WC-HEA Cemented Carbide Based on the CoCrFeNiMn High Entropy Alloy. *J. Alloys Compd.* **2018**, *746*, 1–8. [CrossRef]
36. Yadav, S.; Zhang, Q.; Behera, A.; Haridas, R.S.; Agrawal, P.; Gong, J.; Mishra, R.S. Role of Binder Phase on the Microstructure and Mechanical Properties of a Mechanically Alloyed and Spark Plasma Sintered WC-FCC HEA Composites. *J. Alloys Compd.* **2021**, *877*, 160265. [CrossRef]
37. Gulliver, G.H. The Quantitative Effect of Rapid Cooling Upon the Constitution of Binary Alloys. *J. Inst. Met.* **1915**, *13*, 120–157.
38. Schaffnit, P.; Stallybrass, C.; Konrad, J.; Stein, F.; Weinberg, M. A Scheil-Gulliver Model Dedicated to the Solidification of Steel. *Calphad* **2015**, *48*, 184–188. [CrossRef]
39. *ASTM B311−17*; Test Method for Density of Powder Metallurgy (PM) Materials Containing Less Than Two Percent Porosity. ASTM International: West Conshohocken, PA, USA, 2017.
40. *ASTM C1327-15*; Standard Test Method for Vickers Indentation Hardness of Advanced Ceramics. ASTM International: West Conshohocken, PA, USA, 2024.
41. Tong, C.J.; Chen, Y.L.; Chen, S.K.; Yeh, J.W.; Shun, T.T.; Tsau, C.H.; Lin, S.J.; Chang, S.Y. Microstructure Characterization of AlxCoCrCuFeNi High-Entropy Alloy System with Multiprincipal Elements. *Metall. Mater. Trans. A Phys. Metall. Mater. Sci.* **2005**, *36*, 881–893. [CrossRef]

42. Zheng, H.; Chen, R.; Qin, G.; Li, X.; Su, Y.; Ding, H.; Guo, J.; Fu, H. Microstructure Evolution, Cu Segregation and Tensile Properties of CoCrFeNiCu High Entropy Alloy during Directional Solidification. *J. Mater. Sci. Technol.* **2020**, *38*, 19–27. [CrossRef]
43. Xu, M.; Han, L.; Shen, C.; Jiang, Q.; Yang, G.; Tang, C.; Gharbi, A.; Xu, W.; Yi, J. Impact of 3d TM Elements on Cu Segregation in CrCuTiV-Based High Entropy Alloys and Their Mechanical Properties. *Vacuum* **2024**, *219*, 112723. [CrossRef]
44. Chychko, A.; García, J.; Collado Ciprés, V.; Holmström, E.; Blomqvist, A. HV-KIC Property Charts of Cemented Carbides: A Comprehensive Data Collection. *Int. J. Refract. Met. Hard Mater.* **2022**, *103*, 105763. [CrossRef]
45. Goncharov, I.; Mariani, M.; De Gaudenzi, G.P.; Popovich, A.; Lecis, N.; Vedani, M. Effects of Sinter-HIP Temperature on Microstructure and Properties of WC–12Co Produced Using Binder Jetting. *Metals* **2024**, *14*, 132. [CrossRef]
46. Garcia, J.; Chychko, A.; Gold, C. Design of novel sustainable cemented carbides strengthened by η-phase to replace critical raw materials. *Int. J. Refract. Met. Hard Mater.* **2026**, *138*, 107695. [CrossRef]